Materials Today 98 (2026) 103380

Contents lists available at ScienceDirect

Materials Today

journal homepage: www.elsevier.com/locate/mattod

Glucose-powered bioelectronic patches with a maze-like oxygen-limiting structure accelerate diabetic wound healing

Ming Yin [a,b,c,e,1], Xiangxiang Wang [b,f,1], Engui Wang [e], Longfei Li [b,f], Chang Zhu [b,f], Peng Cheng [b,f], Haochen Xie [f], Han Ouyang [b], Hongqing Feng [e], Shumin Liu [c,*], Zhou Li [a,d,*], Lingling Xu [b,*]

[a] Vita Tech Innovation Center, Beijing Tsinghua Changgung Hospital, School of Clinical Medicine, Tsinghua Medicine, Tsinghua University, Beijing 100084, China
[b] School of Nanoscience and Engineering, University of Chinese Academy of Sciences, Beijing 101408, China
[c] School of Materials Science and Engineering, North China Institute of Aerospace Engineering, Langfang 065000, China
[d] School of Biomedical Engineering, Tsinghua Medicine, Tsinghua University, Beijing 100084, China
[e] College of Materials Science and Opto-Electronic Technology, University of Chinese Academy of Sciences, Beijing 101400, China
[f] Beijing Institute of Nanoenergy and Nanosystems, Chinese Academy of Sciences, Beijing 101400, China

ARTICLE INFO

Keywords:
Glucose fuel cells
Flexible electronic patch
Maze-like oxygen-limiting structure
Diabetic wound healing

ABSTRACT

The hyperglycemic environment in diabetic patients weakens the endogenous electric field at the wound site, hindering healing and leading to chronic non-healing ulcers. This study proposes a glucose-powered bioelectronic patch (GBP) designed to utilize endogenous glucose to generate electrical energy and restore the electric field at the wound edge, thereby promoting healing and improving therapeutic outcomes. We construct a three-dimensional flexible electrode framework using bacterial cellulose (BC), which efficiently fixes platinum particles and absorbs local tissue fluid to facilitate platinum-catalyzed reactions. Additionally, a maze-like oxygen-limiting structure is introduced to enable selective reactions of glucose and oxygen at the anode/cathode, optimizing the reaction interface and mass transport. The GBP achieve a peak power density of 96.57 μW cm^{-2} and can maintain stable high-voltage output for nearly one week, with a performance retention rate of approximately 87% of the initial value. In a diabetic wound model, the patch enhances the endogenous electric field and synergistically exerts multiple biological functions including antibacterial, anti-inflammatory, and anti-adhesion effects, significantly accelerating the wound repair process. This study not only improves the electrical output performance of abiotic-catalyzed glucose fuel cells (GFCs) but also provides new insights into endogenous energy-based electrical stimulation therapy. It holds important reference value for the development of self-powered bioelectronic devices and the clinical management of diabetic non-healing wounds.

Introduction

Globally, diabetes and its associated complications are emerging as an increasingly severe public health challenge. Clinical studies indicate that approximately 15−25% of diabetic patients develop foot ulcers [1–3]. These wounds heal slowly, are prone to infection, and significantly increase the risk of amputation [4]. Severely impacting their quality of life and imposing a heavy socioeconomic burden.

Persistent hyperglycemia in diabetic wounds easily induces chronic inflammation and recurrent infections, suppresses fibroblast proliferation and collagen synthesis, impairs endothelial cell function, disrupts angiogenesis, and dysregulates immune cells such as macrophages. At the same time, endogenous electric fields are significantly weakened. These factors collectively creating a hostile microenvironment that obstructs tissue repair, causing the wounds to trapped in a prolonged inflammatory phase, preventing them from progressing smoothly into the proliferation and remodeling stages [5]. Therefore, actively intervening to remodel the wound microenvironment has become a central focus in the treatment of diabetic wounds. Traditional dressings generally provide protection by covering the wound, but they fail to fundamentally improve the pathological microenvironment caused by local hyperglycemia, leading to issues such as limited functionality and secondary

* Corresponding authors.
E-mail addresses: liushumin100@nciae.edu.cn (S. Liu), li_zhou@tsinghua.edu.cn (Z. Li), xulingling@ucas.ac.cn (L. Xu).
[1] Both authors contributed equally to this work.

https://doi.org/10.1016/j.mattod.2026.103380
Received 10 February 2026; Received in revised form 28 April 2026; Accepted 9 May 2026

damage from dressing removal [6,7]. These limitations result in suboptimal treatment outcomes. Therefore, developing an efficient, safe, and actively regulating treatment strategy for diabetic wounds has become a key research direction in the fields of medicine and biomaterials.

In recent years, electrical stimulation therapy has attracted considerable interest due to its significant potential in promoting tissue repair. Studies have shown that exogenous electrical stimulation can simulate and enhance endogenous electrical signals, thereby promoting the migration of keratinocytes, fibroblasts, and endothelial cells, improving collagen deposition and angiogenesis [8,9]. Furthermore, electrical stimulation regulates the migration and activation of immune cells, modulating the inflammatory response at the wound site, thus promoting wound closure [10,11]. However, despite the promising outlook for electrical stimulation therapy, conventional devices frequently rely on external power sources, which poses challenges such as limited portability, safety concerns, and inadequate control precision.

With advances in flexible electronics [12] and bioenergy harvesting technologies [13], flexible self-powered devices provide new opportunities for diabetic wound management [14]. Among these, thermoelectric devices require a temperature gradient [15], photovoltaic devices rely on external light sources [16], and mechanical energy-driven technologies, such as triboelectric [17,18] and piezoelectric systems [19], require mechanical force stimulation. However, the wound environment often fails to provide the ideal power sources, leading to instability and unsustainability, which limits their widespread clinical application.

Glucose fuel cells (GFCs), as an emerging bioenergy conversion technology, can utilize the glucose abundantly present in bodily fluids as a fuel, generating stable electric field continuously through electrochemical reactions [20–22]. Notably, while generating electricity, GFCs can also effectively lower local glucose concentrations, offering unique therapeutic advantages for hyperglycemia-associated diabetic wounds [23]. However, electrical stimulation alone is insufficient to address the complex microenvironment of diabetic wounds. An ideal wound patch should exhibit multifunctionality: possessing strong antimicrobial properties to combat drug-resistant bacterial infections in the high-glucose environment, anti-inflammatory effects to mitigate persistent inflammation and anti-adhesive characteristics to prevent secondary damage [24,25].

Based on the considerations above, this study presents a flexible glucose-powered bioelectronic patch (GBP). (Fig. 1A-B). The GBP employs in situ reduction technology and electrochemical co-deposition to fabricate platinum nanoparticles (PtNPs) and deposited PtNPs (DPtNPs) on a BC three-dimensional scaffold, constructing a maze-like oxygen-limiting structure. It harnesses glucose in the tissue fluid as its driving force, selectively catalyzing glucose oxidation reactions at the anode and oxygen reduction reactions at the cathode, generating a stable and safe electric field at the wound site. The main body of the dressing uses a bacterial cellulose (BC) scaffold, which provides anti-adhesive

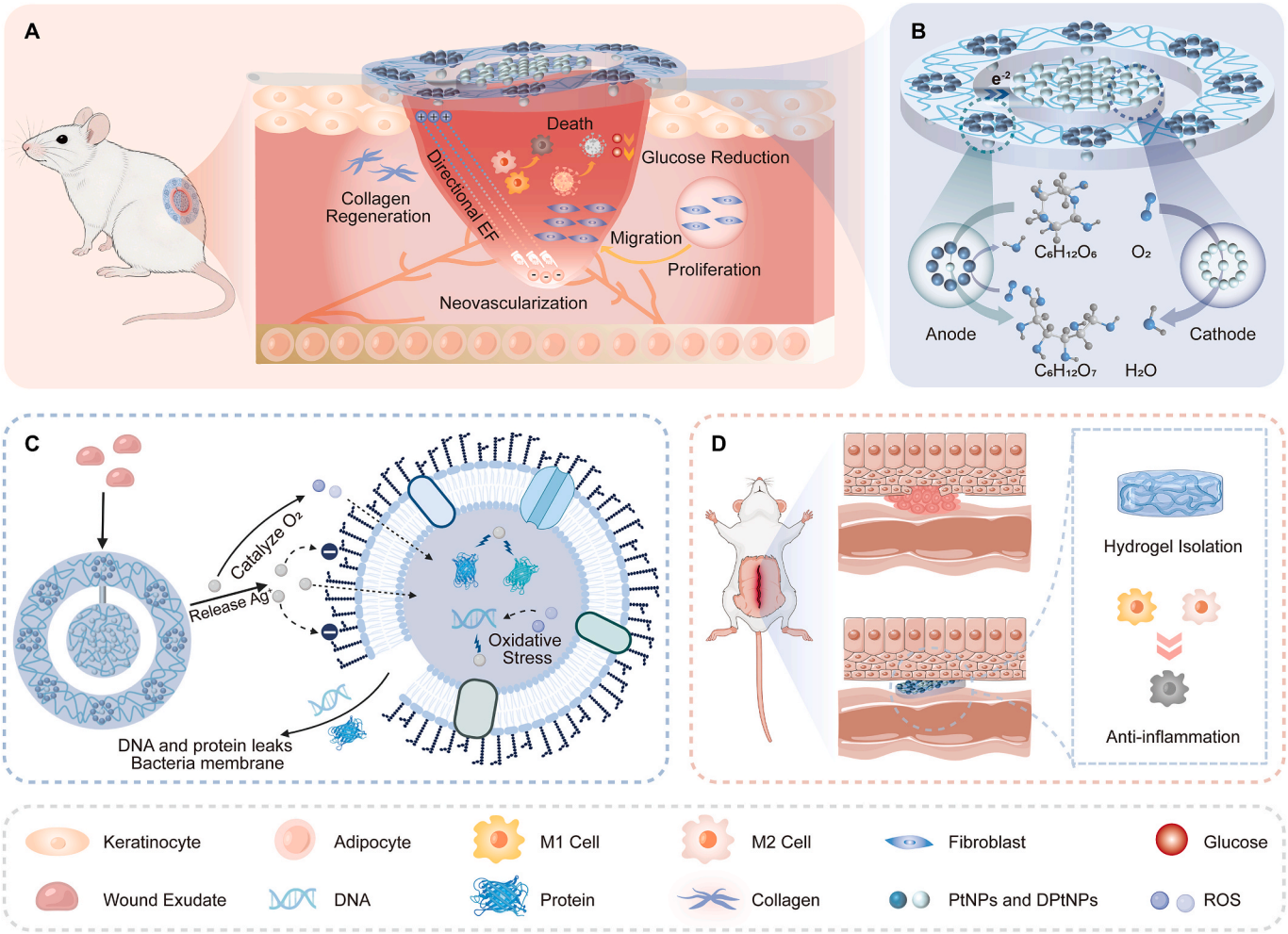

Fig. 1. Flexible GBP enhances endogenous electric fields, synergistically promoting antibacterial, anti-inflammatory, and anti-adhesion effects to accelerate the healing of diabetic wounds. (A) Schematic illustration of a self-powered GFC-based GBP for the treatment of diabetic wounds. (B) Schematic diagram of the working principle of the GBP. (C) Schematic illustration of the antimicrobial mechanism of the patch. (D) Schematic illustration of the anti-adhesion mechanism of the patch.

properties to prevent secondary damage. The silver-plated back layer acts as the electrode, ensuring efficient electronic conductivity while continuously releasing Ag ions to exhibit antimicrobial properties and reduce the risk of wound infection. The GBP can conform to irregular wound surfaces, enhance endogenous electric fields, and combine antimicrobial, anti-inflammatory, and anti-adhesive effects, actively improving the microenvironment of chronic diabetic wounds and promoting healing. As a self-powered, active repair strategy that does not rely on external power sources, the GBP can enhance the quality and speed of wound healing, overcoming the limitations of current clinical treatments for hard-to-heal wounds such as diabetic foot ulcers, and has broad clinical application prospects.

Results and discussion

Preparation and characterization of electrode patch

To construct flexible and efficient electrodes for GFCs, Ag/DPtNPs/BC/PtNPs (ADBP) anodes and Ag/DPtNPs/BC (ADB) cathodes were fabricated. BC, with its three-dimensional porous architecture, was employed as the scaffold due to its ability to support metal catalyst anchoring and facilitates electron and mass transport. The electrodes fabrication process is illustrated in Fig. 2A. For the anode, BC/PtNPs were synthesized via a multistep in situ reduction process and freeze-dried to completely remove residual moisture. A silver layer was then deposited on the surface via magnetron sputtering to serve as the current collector, resulting in the ABP electrode. For the cathode, a pretreated BC membrane was used to construct the AB electrode using the same freeze-drying and sputtering process. Subsequently, the ABP and AB electrodes were individually immersed in the mixed electrolyte for electrochemical co-deposition of DPtNPs (Fig. S4), ultimately producing the ADBP anode and ADB cathode.

In the ADBP anode, the BC/PtNPs layer served as the diffusion layer, facilitating the continuous capture and consumption of trace dissolved oxygen. In contrast, the subsequently DPtNPs acted as the primary catalytic sites for glucose oxidation, thereby driving the anodic reaction and enabling a clear functional separation between mass transport regulation and electrochemical catalysis (Fig. S1A). In the ADB cathode, the same DPtNPs served as an oxygen reduction layer, facilitating efficient cathodic oxygen reduction reactions (Fig. S1B). This design effectively integrates both catalytic and diffusion layers, enhancing the performance of GFCs by ensuring efficient glucose oxidation at the anode and oxygen reduction at the cathode.

Fig. 2B presents a scanning electron microscope (SEM) image of the BC/PtNPs membrane. The BC matrix exhibits a layered, three-dimensional network structure that facilitates the uniform distribution of catalytically active PtNPs. The uniform dispersion of PtNPs is further confirmed by the magnified SEM image (Fig. 2C) and corresponding energy dispersive X-ray spectroscopy (EDS) maps (Fig. 2D) Statistical analysis of the enlarged SEM images indicates an average size of 74.0 ± 21.4 nm (Fig. 2E). Moreover, the mass fraction of PtNPs in the BC/PtNPs membrane is approximately 75.8% (Fig. S2).

To further characterize the prepared BC/PtNPs, X-ray diffraction (XRD) patterns were analyzed. As shown in Fig. 2F, BC exhibits two intense diffraction peaks at 14.5° and 22.7°, along with a minor peak at 16.8°, indicating good crystallinity. After loading PtNPs, the intensity of these peaks decreased, which was attributed to the coverage of BC fibers by PtNPs, acting as active catalytic sites. Simultaneously, five new peaks corresponding to Pt (111), (200), (220), (311), and (222) planes appeared, confirming the successful preparation of Pt with a face-centered cubic (FCC) structure [26].

Furthermore, Fourier Transform infrared spectroscopy (FTIR) (Fig. S3A) of BC/PtNPs shows minimal differences compared to BC, with no new characteristic peaks observed. This suggests that PtNPs has not significantly altered the chemical backbone of BC. The composition and chemical state of BC and BC/PtNPs was further characterized by X-ray photoelectron spectroscopy (XPS). In the full spectrum, C, O, and Pt elements were simultaneously detected in BC/PtNPs (Fig. S3B), consistent with the EDS maps (Fig. 2E). In the high-resolution C 1 s spectrum (Fig. S3C), the broad peak was deconvoluted into three subpeaks: the main subpeak corresponds to the C–O bond, flanked by subpeaks attributed to C=O and C–C bonds in BC, respectively. The intensities of these peaks changed during the preparation of BC/PtNPs, indicating potential interactions between C–O (or C=O) and Pt species during co-reduction. In the high-resolution O 1 s spectrum of BC/PtNPs (Fig. S3D), a subpeak attributable to the Pt–O bond was observed, further supporting the existence of such interactions. Furthermore, the high-resolution Pt 4f spectrum of BC/PtNPs (Fig. 2G) consists of two pairs of subpeaks: 71.6 eV (Pt $4f_{7/2}$) and 74.9 eV (Pt $4f_{5/2}$) for Pt(0), and 72.9 eV (Pt $4f_{7/2}$) and 76.7 eV (Pt $4f_{5/2}$) for Pt(II), indicating that Pt predominantly exists in the zero-valent form with a minor amount of divalent Pt [27,28]. In summary, the oxygen-containing functional groups on the BC surface provide abundant binding sites for PtNPs, forming stable BC/PtNPs composites.

The SEM image of the ADB cathode (Fig. 2H) reveals that micrometer-scale flower-like clusters formed by DPtNPs self-assembly are densely and uniformly anchored on the BC fiber framework. Correspondingly, the EDS maps (Fig. 2I) show that the Pt signal strongly overlaps with the spatial distribution of these micrometer-sized flowers, confirming that the DPtNPs catalytic layer is uniformly and completely formed. Such structures significantly increase the effective electrochemically active surface area of the ADB cathode, enhancing oxygen mass transfer and alleviating cathode polarization. However, excessive accumulation of DPtNPs on the substrate surface may result in an excessively high number of electrochemically active sites on the cathode. This over-aggregation can cause localized increases in glucose concentration near the cathode interface, leading to a rise in the mixed-layer potential and ultimately causing performance degradation of the GFC. Furthermore, trace amounts of Cu, residual from the co-deposition process, remain detectable within the micro-flower structures, further validating the deposition origin of the catalytic layer. Conversely, the DPtNPs catalytic layer on the ADBP anode surface exhibits a porous, microcracked morphology (Fig. 2J). This structure effectively increases the specific surface area and the density of active sites on the ADBP anode, thereby enhancing its catalytic oxidation performance for glucose. The corresponding EDS maps (Fig. 2K) further confirm the uniform dispersion of Pt elements across the entire anode surface, indicating that the DPtNPs catalytic layer achieves high coverage and uniform distribution without agglomeration.

The patches can be precisely customized into specific sizes and shapes, such as circles and squares, demonstrating excellent flexibility that allows GFCs to conform easily to wounds of various locations and complex topographies (Fig. 2L, Fig. S5). Furthermore, considering that the electrode patch need adapt in real time to clinical-grade physiological mechanical signals during wound healing, we calculated the Young's moduli of the ADBP anode and ADB cathode from Fig. 2M to be 2 MPa and 3.8 MPa, respectively. These values are comparable to the modulus of human skin (0.42–107.80 MPa) [29], ensuring dynamic conformal adhesion. Moreover, the swelling curve in Fig. 2N demonstrates the patch's rapid absorption capacity for wound exudate, while the contact angle results in Fig. 2O (all $< 40°$) confirm its excellent hydrophilicity. These properties collectively provide GFC patches with a sustained hydrated microenvironment, facilitating in situ electricity generation by the GFCs.

Performance characterization and validation of electrodes.

Fig. 3A illustrates the hierarchical structure and operating mechanism of the ADBP anode. This anode employs BC as its three-dimensional framework, onto which a silver current collector, a DPtNPs catalytic layer, and an outer PtNPs diffusion layer are prepared. Upon activation, the anode exhibits dual functionality for glucose oxidation and oxygen reduction. The PtNPs diffusion layer leverages the low concentration gradient of dissolved oxygen in body fluids to selectively reduce O_2 to H_2O, thereby creating an oxygen-deficient microenvironment in the

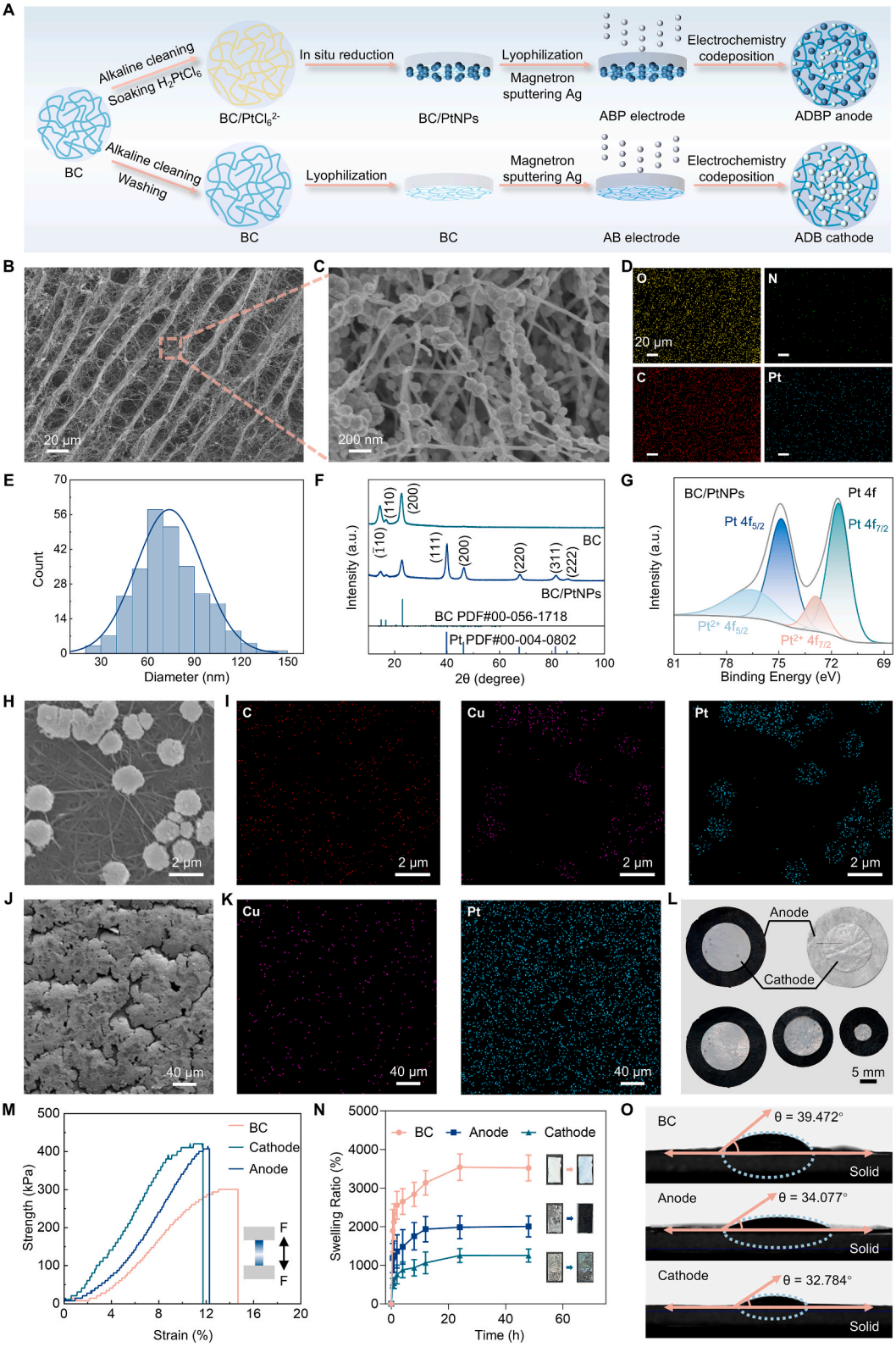

Fig. 2. Preparation and characterization of electrode patch. (A) Schematic diagram of the preparation process of anode and cathode patch. (B) SEM image of the BC/PtNPs electrode membrane. (C) Locally enlarged SEM image of the BC/PtNPs electrode membrane. (D) EDS maps of the BC/PtNPs electrode membrane. (E) Histogram of PtNPs diameter distribution in the locally enlarged SEM image. (F) XRD patterns of the BC and BC/PtNPs electrode membrane. (G) Pt 4f XPS spectra of the BC/PtNPs electrode membrane. (H) SEM image of the ADB cathode. (I) EDS maps of the ADB cathode. (J) SEM image of the ADBP anode. (K) EDS maps of the ADBP anode. (L) GFC patches can be customized to different sizes. (M) Stress–strain curves of BC electrode membranes, ADBP anodes, and ADB cathodes under tensile testing conditions. (N) Swelling properties of BC electrode membranes, ADBP anodes, and ADB cathodes at room temperature in 1 × PBS. (O) Contact angle analysis of BC electrode membranes, ADBP anodes, and ADB cathodes under 1 × PBS conditions.

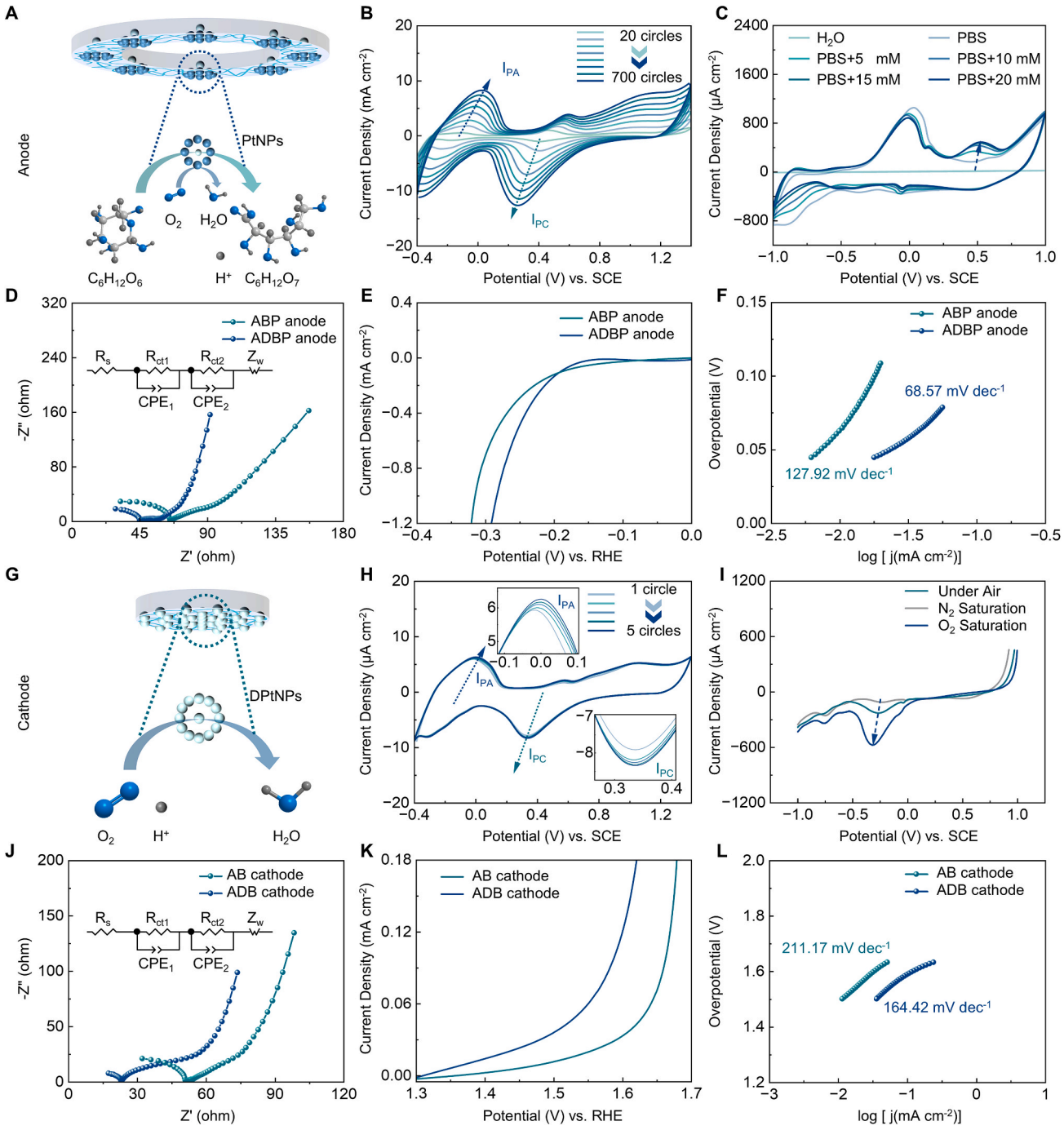

Fig. 3. Performance characterization and validation of electrodes. (A) Schematic of the ADBP anode material, consisting of silver (Ag) nanoparticles, platinum (Pt) nanoparticles (in situ reduced PtNPs), and deposited platinum (Pt) nanoparticles (DPtNPs) immobilized on a BC scaffold. In the diffusion layer of the ADBP anode, a small amount of dissolved oxygen (O_2) is catalyzed by PtNPs to form water (H_2O). Meanwhile, in the catalytic layer deep within the ADBP anode, glucose ($C_6H_{12}O_6$) is catalyzed by DPtNPs to produce gluconic acid ($C_6H_{12}O_7$) and protons (H^+), releasing electrons (e^-) in the process. The glucose oxidation reaction plays a dominant role within the ADBP anode. (B) Evolution of CVs at 50 mV s^{-1}, ranging from 1.40 to −0.40 V vs. SCE, during ADBP anode fabrication, represented by selected CV cycles: 20, 100, 200, 300, 400, 500, 600, and 700. C) Comparison of CVs (scan rate: 10 mV s^{-1}, potential range: 1 to −1 V vs. SCE) in different liquids: H_2O, PBS, and PBS containing 5 mM, 10 mM, 15 mM, and 20 mM glucose. (D) Electrochemical Impedance Spectroscopy (EIS) of ABP and ADBP anodes. (Equivalent circuit models used for impedance analysis of the anode. The Nyquist plots were fitted with this circuit to extract the charge transfer resistance at the electrode–electrolyte interface. R_s, solution resistance; CPE, constant phase angle element; R_{ct}, charge transfer resistance; Z_w, warburg impedance.) (E) Polarization curves, and (F) Tafel slope curves of ABP and ADBP anodes. (G) Schematic of the ADB cathode material, consisting of silver (Ag) nanoparticles, and deposited platinum (Pt) nanoparticles (DPtNPs) immobilized on a BC scaffold. The DPtNPs catalyze the reduction of protons (H^+) and dissolved oxygen (O_2) to water (H_2O). (H) Evolution of CVs at 50 mV s^{-1}, ranging from 1.40 to −0.40 V vs. SCE, during ADB cathode fabrication, represented by selected CV cycles: 1, 2, 3, 4, and 5. I) Comparison of LSVs (scan rate: 10 mV s^{-1}, potential range: 1 to −1 V vs. SCE) of ADB cathodes saturated with air, nitrogen (N_2), and oxygen (O_2) in 1 × PBS. (J) Electrochemical Impedance Spectroscopy (EIS) of AB and ABD cathodes. (The equivalent circuit models for the cathode and anode are identical.) (K) Polarization curves, and (L) Tafel slope curves of AB and ADB cathodes.

inner layer. Simultaneously, glucose penetrates the diffusion layer via the concentration gradient, reaching the DPtNPs catalytic layer where it is oxidized to gluconic acid ($C_6H_{12}O_7$), releasing e^- and H^+. Consequently, the anode potential is primarily driven by the glucose oxidation reaction ($C_6H_{12}O_7 + H_2O \rightarrow C_6H_{12}O_7 + 2H^+ + 2e^-$). This "maze-like oxygen-limiting" structure enables a highly selective, self-powered bioelectrochemical process within the ADBP anode. Furthermore, we validated this mechanism by performing cyclic voltammetry (CV) tests on ABP and ADBP anodes (Fig. S6). While the ABP anode initially exhibited oxygen reduction characteristics, the ADBP anode predominantly shifted to glucose oxidation characteristics after the introduction of DPtNP. We also conducted CV testing on the ADBP anode in PBS containing varying glucose concentrations (Fig. 3C). As the glucose concentration increased, a distinct glucose oxidation peak appeared around 0.5 V (vs. SCE), with its peak current density rising. Simultaneously, the intensity of the characteristic peak near 0 V (vs. SCE) gradually decreased. This peak is attributed to the insertion and de-insertion of solution ions within the porous BC/PtNPs membrane. The glucose oxidation peak consistently dominated, while a faint oxygen reduction current was also observed in the cathodic current component, further confirming the functional feasibility and selectivity of this structure under physiological conditions. Moreover, as shown in Fig. S7A and S7B, the peak current increases with the scan rate. Both the anodic peak current (I_{PA}) and the cathodic peak current (I_{PC}) exhibit a linear correlation with the square root of the scan rate. This indicates that glucose undergoes free diffusion within the ADBP electrode and that the anodic reaction is diffusion-controlled. The DPtNPs catalytic layer of the ADBP anode was fabricated using CV (Fig. 3B). As the number of deposition cycles increased, the peak current density in the CV curves steadily rose, indicating continuous nucleation and growth of DPtNPs on the BC three-dimensional framework. Additionally, the peak current shown in Fig. S8A exhibits a strong linear relationship with the number of deposition cycles, further confirming the uniform and continuous growth of DPtNPs. Subsequently, we employed electrochemical impedance spectroscopy (EIS) to evaluate the interfacial impedance of the ADBP and ADB anodes (Fig. 3D). The introduction of the DPtNPs catalytic layer significantly reduced the charge transfer resistance of the ADBP anode, indicating substantially enhanced interfacial electron transfer kinetics. Linear sweep voltammetry (LSV) further revealed the polarization curves of both electrodes (Fig. 3E), with the ADBP anode exhibiting a lower overpotential during glucose oxidation. And the taffel slope curves (Fig. 3F) showed that the Tafel slope of the ADBP anode was 68.57 mV dec^{-1}, which is lower than that of the ADB anode, indicating faster reaction kinetics and superior electrocatalytic performance. Collectively, these results validate the high efficiency of the ADBP anode in glucose oxidation systems.

However, the ADB cathode utilizes a BC framework to sequentially prepare a silver current collector and a DPtNPs catalytic layer, which catalyzes the oxygen reduction reaction: $1/2O_2 + 2H^+ + 2e^- \rightarrow H_2O$ (Fig. 3G). This pathway exhibits a lower Gibbs free energy compared to the direct reaction between O_2 and glucose, making it thermodynamically more favorable [30,31]. The CV curve confirms that dissolved oxygen reaches the active sites of DPtNPs through diffusion-controlled transport and undergoes reduction (Fig. S7C-D). Furthermore, the successful preparation of the DPtNPs catalytic layer is demonstrated by SEM images and electrodeposition CV curves (Fig. 2H, Fig. 3H, Fig. S8B). Considering the oxygen reduction reaction occurring at the cathode, we conducted LSV tests on the ADB cathode in PBS solutions under different saturated atmospheres (air, N_2, and O_2) (Fig. 3I). Characteristic peaks indicative of oxygen reduction was observed in both air and O_2 environments, with a more pronounced signal in O_2, demonstrating the ADB cathode's specific response to oxygen. We further evaluated the performance of the AB and ADB cathodes using EIS, which revealed a significant reduction in charge transfer resistance after incorporating DPtNPs (Fig. 3J). Polarization curves (Fig. 3K) and Tafel slope plots (Fig. 3L) show that the ADB cathode exhibits lower overpotentials and a reduced Tafel slope of 164.42 mV dec^{-1}, confirming its faster reaction kinetics and enhanced catalytic activity for oxygen reduction.

Characterization and performance analysis of the GFCs.

Coupling the ADBP anode with the ADB cathode forms a complete GFC (Fig. 4A, Fig. S9). This device can be integrated into an animal's energy system and stably generates electrical energy in PBS containing 1–15 mM glucose. To verify the energy source, we conducted Open Circuit Potential-Time (OCP-T) tests on the ADB cathode, ADBP anode, and GBP (Fig. S10). The results indicate a sufficient potential difference between the ADB cathode and the ADBP anode, which serves as the voltage source for the GBP. Additionally, we performed the same test on GFCs with a non-oxygen-limiting structure (Fig. S11), and the results showed a significant reduction in output voltage. These findings further confirm the advantages of the maze-like oxygen-limiting structure. Furthermore, as shown in Fig. 4B, the open-circuit voltage (OCV) increases with rising glucose levels, peaking at approximately 675 mV at 5 mM. Within the 1–5 mM range, the OCV exhibits a linear relationship with glucose concentration (Fig. 4C). When glucose concentration exceeds 5 mM, the OCV tends to plateau or slightly decline, which is attributed to glucose saturation at the catalytic site and adsorption poisoning of the active site by intermediate products. Considering that GFCs need to function effectively in a diabetic wound model, we placed them in an open system containing PBS with 15 mM glucose and conducted OCV testing over nearly one week (Fig. 4D). The stable OCV output indicates that oxygen consumption did not cause obvious output instability under the tested conditions, suggesting that oxygen supply was sufficient to maintain the coupled anodic and cathodic reactions during operation. After 6 days, the device still produced 432 mV, retaining 87% of its initial performance (Fig. S12), demonstrating the long-term stability of the GFC. Further testing using an electrochemical workstation evaluated power density (Fig. 4E, Fig. 4F) and polarization curves (Fig. 4G) across varying glucose concentrations. The results show that OCV, current density, and peak power density all depend on glucose concentration (Fig. S13A-C), with the optimal peak power density reaching approximately 96.57 μW cm^{-2} at 5 mM glucose—one of the highest values reported to date for implantable non-biocatalytic GFCs (Fig. 4J) [32–40]. When the concentration increased to 15 mM, both the peak power density (Fig. S14A) and current density (Fig. S14B) decreased slightly, further confirming the partial deactivation of active sites due to product adsorption. Additionally, impedance matching tests on the GFC revealed that variations in load resistance significantly affect its peak output voltage and current. When the GFC is connected to an external load, the output voltage increases with rising load resistance, while the output current decreases correspondingly (Fig. 4H). The GFC achieves its maximum peak power output at a load resistance of approximately 8 kΩ (Fig. 4I). Notably, wound tissue resistance typically ranges from several hundred to several thousand ohms. Within this impedance range, the voltage and current output by the GFC can generate effective electrical stimulation for diabetic wounds. Collectively, these results confirm that this GFC delivers both high power output and reliable stability within physiological glucose ranges, establishing an experimental foundation for sustained energy supply in diabetic models.

Evaluation of the biocompatibility and antibacterial properties of patches.

Given that the GBP comes into direct contact with the wound, its biocompatibility must be verified beforehand. We assessed the toxicity of each patch group on NIH3T3 cells using live/dead staining (Fig. 5A) and Cell Counting Kit-8 assays (Fig. 5B). The results showed that cell viability in all patch groups reached approximately 100%, showing no significant difference compared to the blank group, further confirming the non-cytotoxicity of the materials. Furthermore, in the diabetic mouse model, blood routine examinations conducted on day 15 post-surgery (Fig. 5C) revealed no statistically significant differences in key hematological parameters—including white blood cell (WBC), red blood cell (RBC), platelet (PLT) counts, and monocyte (Mon) levels—among

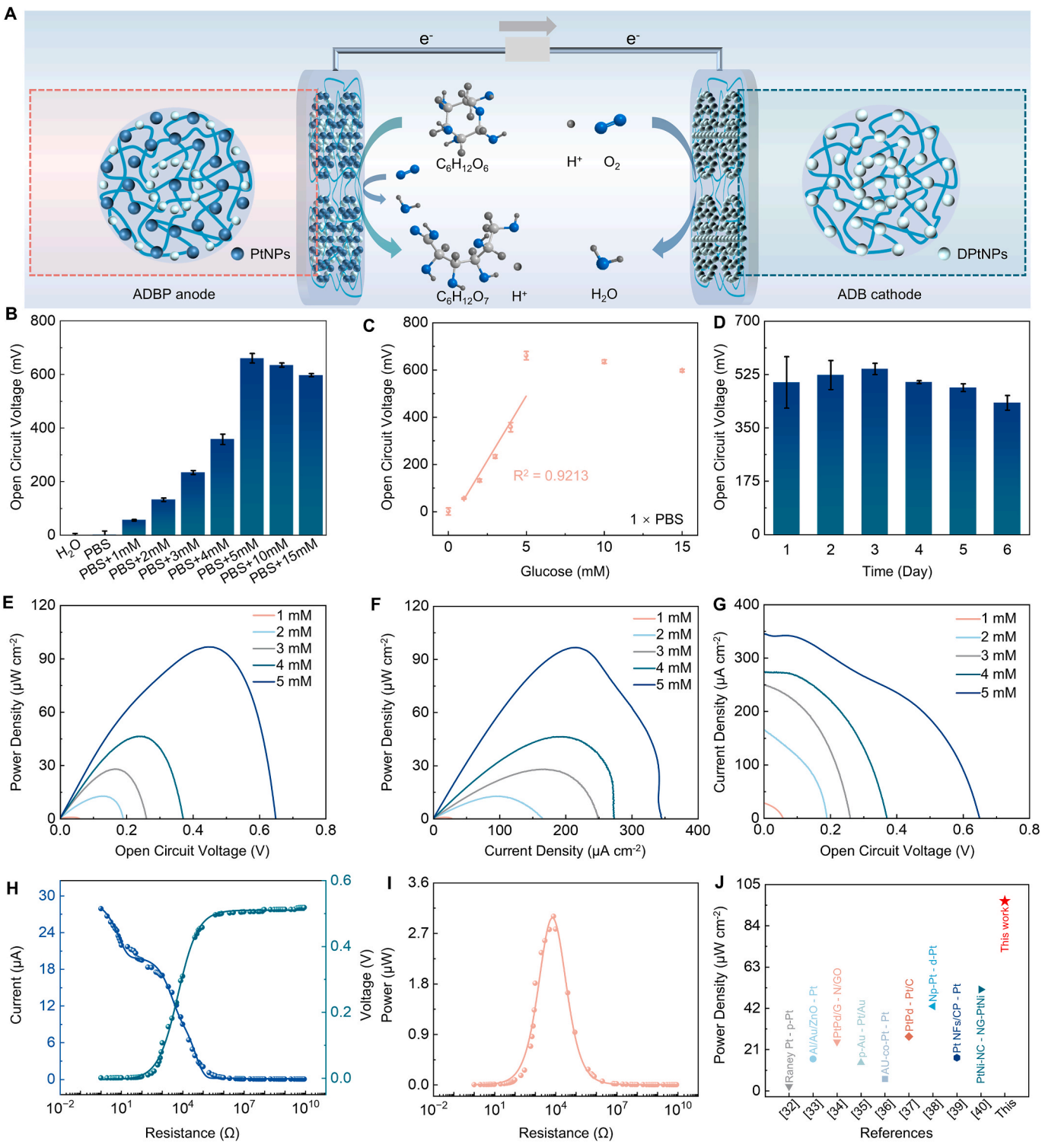

Fig. 4. Characterization and performance analysis of the GFCs. (A) Schematic diagram of GFC power generation. (B) Open-circuit voltage variations of GFCs in different solutions: H_2O, PBS, and PBS containing 1 mM, 2 mM, 3 mM, 4 mM, 5 mM, 10 mM, and 15 mM glucose. (C) The correlation of open-circuit voltage of GFCs on glucose concentration in PBS. (D) Long-term testing of GFCs in PBS containing 15 mM glucose. GFCs at different glucose concentrations (1, 2, 3, 4, and 5 mM): (E) Power density versus open-circuit voltage, (F) Power density curve, and (G) Polarization curve. Impedance-matching test: The variation of (H) voltage, current, and (I) power of GFCs with different external load resistances. (J) Peak power density of the GFC compared with those reported in other studies.

the BC group, All-Materials (AMs) group, GBP group, and Blank group. Additionally, H&E staining of major organs (heart, liver, spleen, lung, and kidney) (Fig. S15) showed no inflammatory infiltration, necrosis, or fibrotic lesions, further indicating the excellent biocompatibility of the patches [41].

Bacterial infections are a major cause of delayed healing in diabetic wounds, making the antimicrobial properties of the patch crucial. We evaluated the inhibitory effects of BC, BC/PtNPs, AMs, and GBP against *S. aureus* and *E. coli* (Fig. 5D). Specifically, the AMs patch achieved kill rates of 98.37% against *S. aureus* and 96.05% against *E. coli,* while the

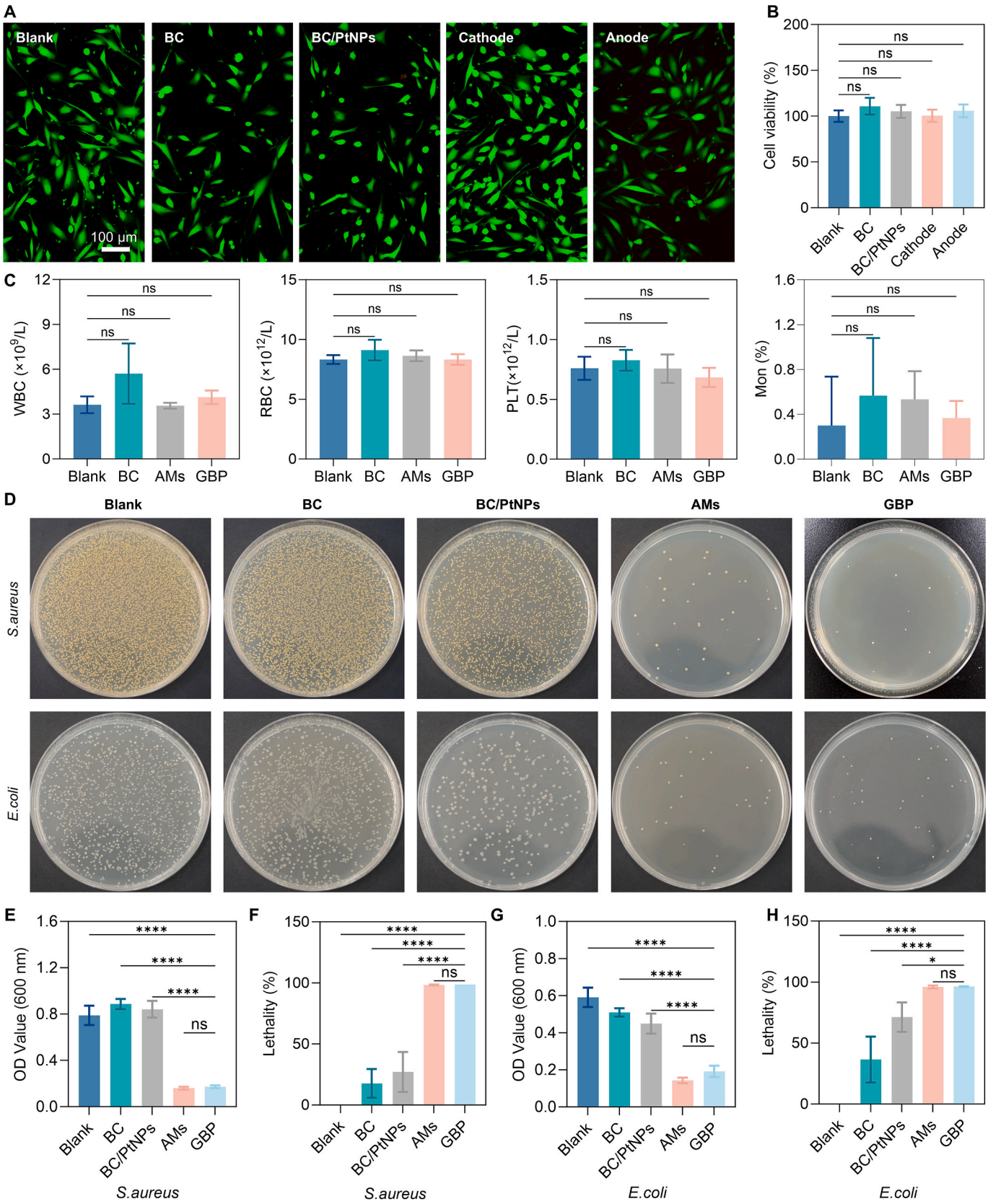

Fig. 5. Evaluation of the biocompatibility and antibacterial properties of patches composed of different components. (A) Live/dead cell staining images of NIH3T3 cells cultured with different patches after 2 days. Scale bars: 100 μm. (B) The corresponding cell viability of different patches evaluated by the CCK-8 test (n = 3). (C) Blood routine examination of mice treated with different groups on Day 15 (n = 3). (D) Photographs of different patches against *E. coli* and *S. aureus*. (E) OD values, and (F) the corresponding mortality of *S. aureus* with different patches. (n = 3) G) OD values, and H) the corresponding mortality of *E. coli* with different patches. Data are presented as mean ± SD, and statistical significance is determined by one-way ANOVA; *p < 0.05, ****p < 0.0001; ns, not significant.

GBP exhibited comparable antibacterial efficiencies of 98.74% and 96.30% respectively (Fig. 5F, Fig. 5H), with no significant difference between the two groups. Furthermore, the colony count results corresponded with the respective OD values (Fig. 5E, Fig. 5G), further confirming the strong antibacterial properties of the AMs and GBP groups. In contrast, the BC and BC/PtNPs group, which lacked Ag components, showed negligible antibacterial activity. These results indicate that the antibacterial efficacy of the patch was primarily associated with the introduction of Ag rather than electrical stimulation. In both AMs and GBP, the magnetron-sputtered Ag layer could serve as a sustained Ag^+ source in the wound microenvironment, thereby providing the main basis for their robust and stable antibacterial performance. Mechanistically, the released Ag^+ can electrostatically interact with negatively charged bacterial cell membranes, disrupting membrane integrity and promoting intracellular ROS generation, ultimately leading to bacterial inactivation (Fig. 1C) [42].

Anti-adhesion performance of the patch.

Traditional dry wound dressings such as gauze were prone to adhere to wound surfaces, which not only increased the mechanical tearing damage to newly formed tissue during dressing changes but also provoked chronic inflammatory responses. Therefore, an ideal wound patch needed to cooperatively establish a triple barrier of physical isolation, antimicrobial action, and anti-inflammation within the same interface to achieve comprehensive intervention (Fig. 1D). In this study, the anti-adhesion performance of the patch was systematically evaluated using a standardized peritoneum–mesentery injury model. Fig. 6A illustrates the detailed surgical procedure. Briefly, uniform pinpoint bleeding was induced by mechanical stimulation on the surfaces of the peritoneum and mesentery. Subsequently, the blank group received suturing only without additional intervention, whereas the BC and AMs groups underwent implantation of sterile patches between the injured peritoneum and mesentery followed by suturing (Fig. 6B).

Firstly, the surface of the patch exhibits a highly hydrophilic and hydrated interfacial characteristic, which can effectively reduce nonspecific adsorption of proteins and bacteria [43,44]. Contact angle analysis (Fig. 2O) confirmed that the patch surface was highly hydrophilic, supporting the formation of a hydrated interfacial layer that helps prevent the initial attachment of microorganisms and cells [45].

Moreover, on postoperative day 3, gross inspection of intraperitoneal adhesions showed that the Blank group exhibited tight and continuous fibrous connections between the peritoneum and mesentery, with difficult tissue separation. In contrast, after patch intervention in both the BC and AMs groups, the mesentery and surrounding tissues were readily separable (Fig. 6C). Additional analysis using Nair's adhesion score further demonstrated that both the BC and AMs groups significantly reduced adhesion severity, indicating reliable anti-adhesion efficacy (Fig. 6D).

At the histological level, H&E staining confirmed marked inflammatory cell aggregation at the injury interface in the Blank group on postoperative day 3 (Fig. 6E). Quantification revealed that the inflammatory cell density in the Blank group was approximately 292 cells per 0.1 mm^2, whereas it decreased to approximately 126 cells per 0.1 mm^2 and 146 cells per 0.1 mm^2 in the BC and AMs groups, respectively (Fig. 6F). These findings indicate that the presence of BC and AMs patches helps mitigate acute inflammatory responses in injured mesenteric tissues.

To further elucidate the regulatory effects of the patches on the immune microenvironment at the injury interface, we analyzed macrophage infiltration and their functional phenotypes during the early postoperative period. M1 macrophages ($CD86^+$), are typically associated with early pro-inflammatory responses, release of inflammatory mediators, indicating a strong inflammatory mobilization state in the tissue, whereas M2 macrophages ($CD206^+$), associated with tissue repair and fibrosis [24,46,47], and are often significantly increased in the pro-fibrotic microenvironment that drives adhesion formation [48]. Our results show that, for $CD86^+$ macrophages, the BC and AMs groups showed approximately 10.6% and 10.4% infiltration, respectively, much lower than the Blank group (23.7%) (Fig. 6G, H). Similarly, for $CD206^+$ macrophages, the infiltration in the BC and AMs groups was approximately 9.8% and 10.3%, respectively, compared to 22.7% in the Blank group (Fig. 6I, J). No significant difference was observed between the BC and AMs groups for either marker. This suggests that the patches do not simply induce a shift of macrophages from M1 to M2 (or vice versa), but more likely reduce sustained stimulation and cell recruitment at the injury interface, thereby overall weakening the excessive aggregation of early immune cells, and bringing the local immune response closer to a physiological range.

In summary, the anti-adhesion mechanisms of BC and AM patches result from the synergistic effects of physical barriers, hydrated interfacial protection, antibacterial properties, anti-inflammatory actions, and anti-fibrotic effects. These patches not only serve as physical barriers isolating the injured surface but also help reduce nonspecific protein adsorption, initial cell/bacterial attachment, and local inflammatory responses. Consequently, they effectively prevent pathological adhesions following mesenteric injury while promoting orderly tissue repair.

Therapeutic effects of GBP on diabetic wound healing.

To evaluate the wound-healing effects of the GBP in promoting diabetic wound repair via endogenous glucose–powered electrical stimulation, a full-thickness excisional wound model was established on the dorsal skin of diabetic mice (Fig. 7A, Fig. S16, Fig. S21). The Blank group was covered only with a breathable 3 M dressing and served as a self-healing control, whereas the BC, BC/PtNPs, Ag/BC, AMs, OC-GBP, and GBP groups received their respective patches applied directly onto the wound surface, followed by coverage with a 3 M dressing. This experimental design effectively minimized wound contraction, excluded the potential influence of the dressing itself on wound healing, and ensured stable fixation of the patches at the wound site, thereby enabling continuous and reliable treatment.

Following skin injury, the transepithelial potential is disrupted. Consequently, an endogenous electric field (EF) forms from the wound periphery toward the center. During normal wound healing in mice, the potential exhibits a characteristic volcano-like distribution pattern, with higher potentials at the wound periphery and the lowest potential at the center (Fig. 7B). Such endogenous EFs are increasingly recognized as key biophysical cues that guide directional keratinocyte migration and re-epithelialization. However, in diabetes, endogenous electrical signals are often weakened or poorly sustained, contributing to chronic non-healing wounds. Therefore, the ability to reconstruct and maintain a robust wound EF represents a mechanistically meaningful readout for assessing the therapeutic action of the GBP.

Electrical potential measurements showed that the wound potential in Blank group was only approximately 27 mV, while no significant change was observed in the BC group, indicating that simple coverage or isolation is insufficient to effectively restore the electric field. In contrast, the GBP group exhibited a marked increase in the potential to approximately 210 mV, effectively remodeling the endogenous EF. Notably, the potential in the AMs group transiently increased to approximately 98 mV, which can be attributed to the material's inherent local electrochemical activity. The AMs underwent a mild oxidation reaction in the wound microenvironment (e.g., the Ag^+/Ag redox couple), releasing a small number of electrons toward the center of the wound through the BC/PtNPs conductive network, thereby temporarily enhancing the intensity of the endogenous electric field. However, the AMs group did not form a complete electronic circuit; the material had only localized contact with the tissue and lacked a closed circuit. Consequently, the generated charge could not be continuously and directionally transmitted, and the potential decayed to the level of the endogenous electric field within a few minutes (Fig. S17). In contrast, the potential in the GBP group remained stable at approximately 210 mV, indicating that the AMs group cannot provide stable, sustained electrical stimulation output. Furthermore, wound potential was

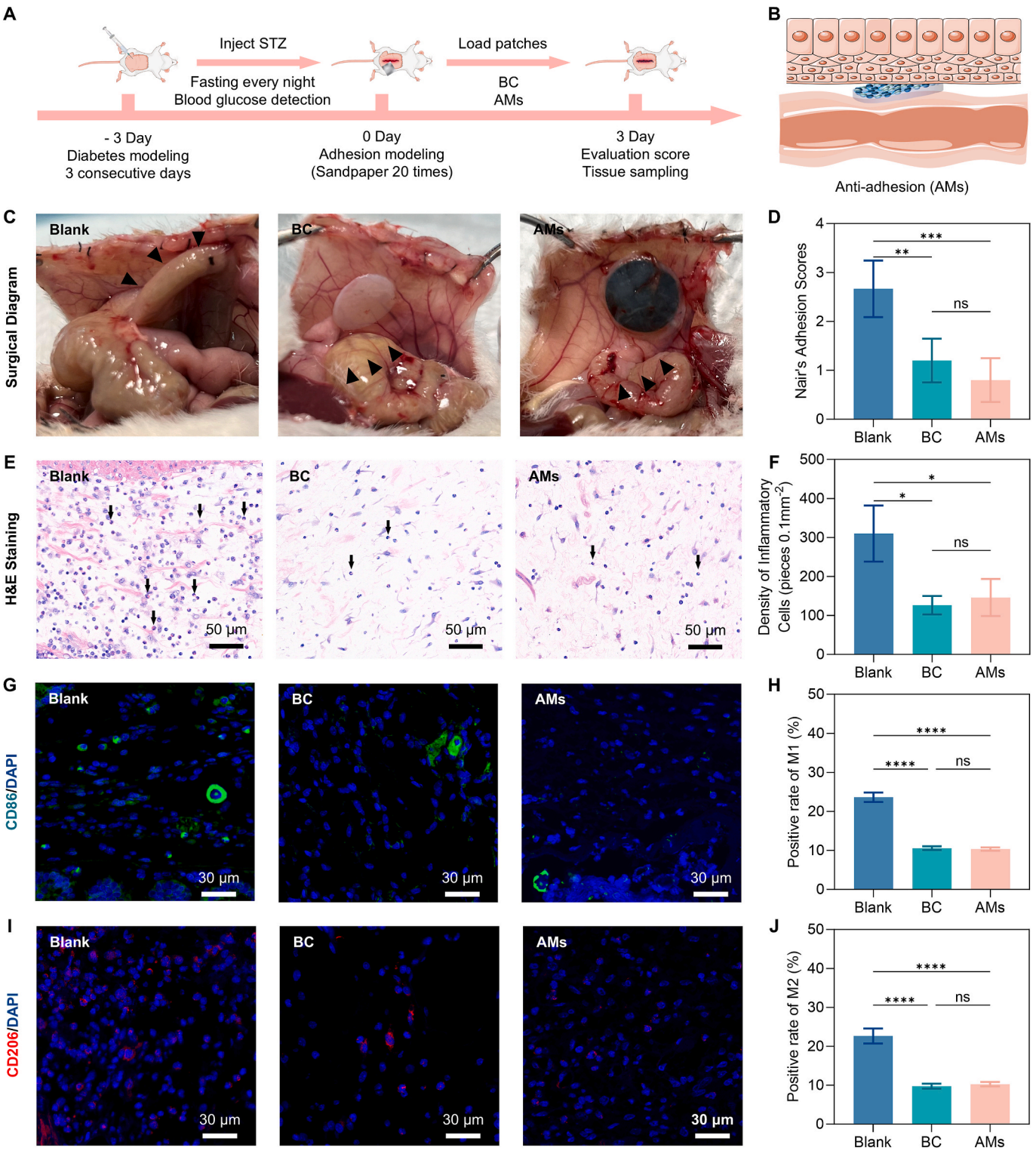

Fig. 6. Effects of the patches on mesentery adhesion and inflammatory response in Diabetic mice. (A) Surgical procedure for characterizing the anti-adhesion properties of patches. (B) Schematic diagram of anti-adhesion for AMs patches. (C) Adhesion status of the mesentery in different groups on the 3rd postoperative day. (D) Nair' s adhesion scores of the different groups ($n \geq 3$). (E) H&E staining of mesentery on the 3rd day. Scale bars, 50 μm; black arrows: neutrophils. (F) Density of inflammatory cells ($n = 3$). (G) Immunofluorescence staining images of CD86 in the mesentery on the 3rd day. Scale bars, 30 μm. (H) Positive rate of M1 macrophages ($n = 3$). (I) Immunofluorescence staining images of CD206 in the mesentery on the 3rd day. Scale bars, 30 μm. (J) Positive rate of M2 macrophages ($n = 3$). Data are presented as mean ± SD, and statistical significance is determined by one-way ANOVA; *$p < 0.05$, **$p < 0.01$, ***$p < 0.001$, and ****$p < 0.0001$; ns, not significant.

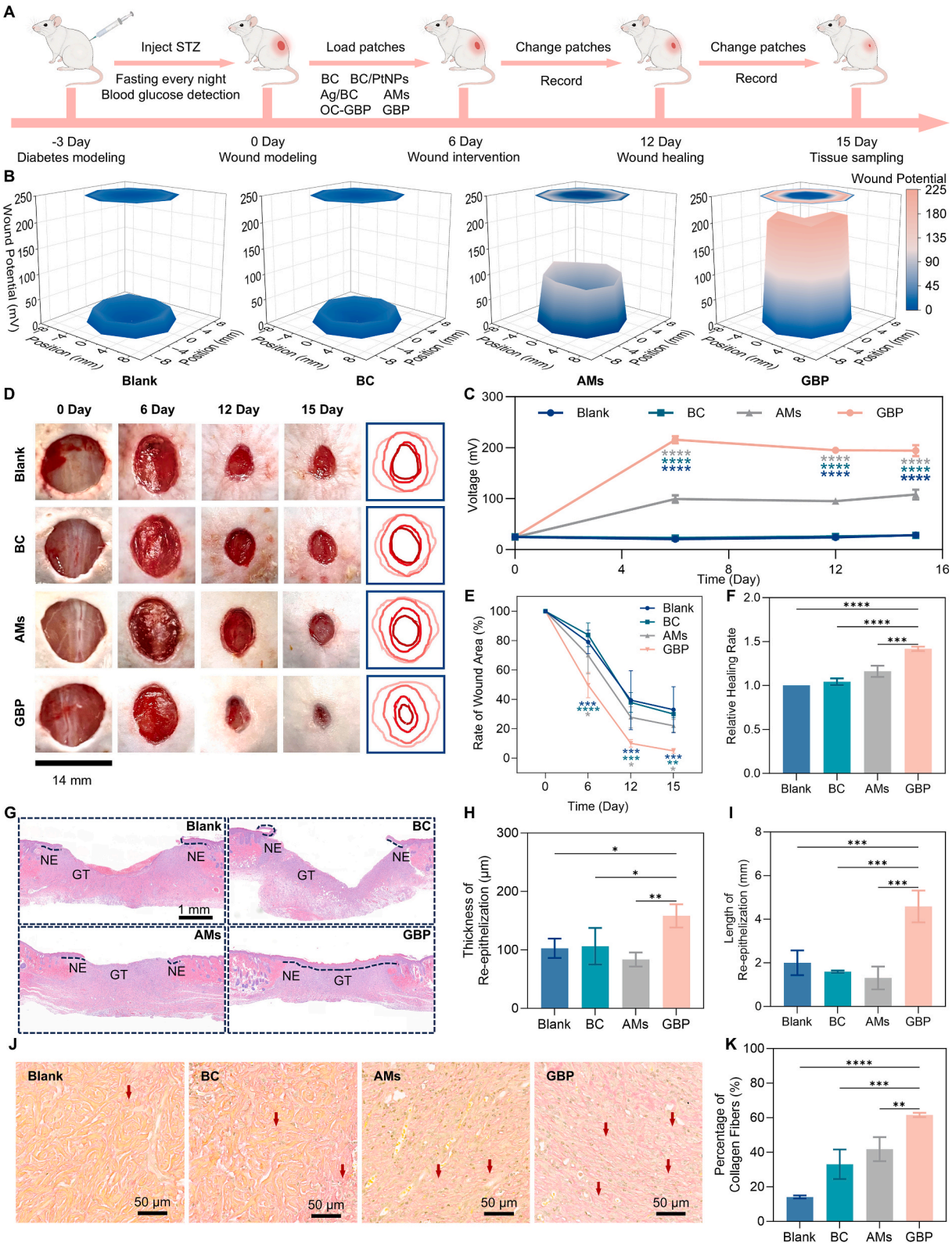

Fig. 7. Analysis of the therapeutic effects of GBP on diabetic wound healing. (A) Timeline of treatment for diabetic wound using the GBP. (B) 3D profile of the wound potential using different patches. (C) Continuous wound potential monitoring throughout the entire experimental process using different patches ($n \geq 3$). (D) Photographs of wound and wound contour using different patches. Scale bars, 14 mm. (E) Rate of wound area ($n = 3$). (F) The relative healing rates of wounds treated with different patches compared to the blank group within 15 days ($n = 3$). (G) H&E staining of wound tissue in different groups. Scale bars, 1 mm; GT: granulation tissue; NE: new epithelium. (H) Thickness of re-epithelization in different groups ($n = 3$). (I) Length of re-epithelization in different groups ($n = 3$). (J) Sirius red staining in the center of the repaired tissue in different groups. Scale bars, 50 μm; red arrows: collagen fiber. (K) Percentage of collagen fibers in different groups ($n = 3$). Data are presented as mean ± SD, and statistical significance is determined by one-way ANOVA; *$p < 0.05$, **$p < 0.01$, ***$p < 0.001$, and ****$p < 0.0001$.

monitored in all groups at every dressing change. The data demonstrated that the GBP group sustained a significantly elevated wound potential compared to the other groups for the duration of the therapy (Fig. 7C, Fig. S22E). This advantage provides a reliable biophysical basis for subsequent electrotactic cell migration and tissue regeneration, explaining the superior therapeutic outcomes of GBP compared to other groups.

Based on the observed EF remodeling, we further assessed its impact on wound closure. Wound images showed that the GBP group consistently exhibited the smallest wound area throughout the healing process (Fig. 7D, Fig. S22A), suggesting that EF enhancement may accelerate re-epithelialization. Quantitative analysis confirmed that on day 6, the wound healing rate in the GBP group reached 50.29%, which was 1.58-, 1.68-, 1.62-, 1.20-, 3.11-, and 2.40-fold faster than those in the OC-GBP group (31.78%) AMs group (30.02%), Ag/BC group (30.99%), BC/PtNPs group (41.95%), BC group (16.09%), and Blank group (20.95%), respectively (Fig. 7E, Fig. S18, and Fig. S22B-C). By day 12, wounds in the GBP group exhibited substantially improved repair (89.93%), which was significantly greater than that in the OC-GBP (70.02%), AMs (72.16%), Ag/BC (61.17%), BC/PtNPs (52.68%), BC (62.12%), and Blank (60.56%) groups (Fig. 7E, Fig. S22B). By postoperative day 15, wounds in the GBP group were nearly completely closed, with a relative healing rate approximately 1.42 times that of the Blank group (Fig. 7F, Fig. S22D).

To correlate macroscopic healing with tissue-level regeneration, we evaluated granulation tissue and re-epithelialization. H&E staining showed that the GBP group exhibited a continuous, fully regenerated epidermal coverage, while the other groups displayed varying degrees of incomplete epithelial coverage or structural discontinuity (Fig. 7G, Fig. S23A). Quantitative analysis further confirmed that both epithelial thickness and length of re-epithelialization were significantly greater in the GBP group compared to all other groups. Specifically, at the time of complete epithelialization in the GBP group, the re-epithelialization thickness in the OC-GBP, AMs, Ag/BC, BC/PtNPs, BC and Blank groups reached only 65.03%, 52.81%, 58.68%, 64.27%, 67.27% and 64.91% of that observed in the GBP group, respectively (Fig. 7H, Fig. S23B). Similarly, the corresponding re-epithelialization lengths were 34.39%, 28.50%, 25.93%, 23.96%, 34.87% and 43.66% of the GBP group (Fig. 7I, Fig. S23C).

In addition to re-epithelialization, high-quality wound repair also relies on granulation tissue formation and extracellular matrix remodelling [49]. Therefore, sirius red staining was employed to assess collagen deposition, which is closely related to the maturation of granulation tissue (Fig. 7J; indicated by red arrows). The GBP group displayed denser and more widespread collagen accumulation, and quantitative assessment revealed that collagen deposition reached 61.63%, significantly higher than AMs (41.82%), BC (33.08%), and Blank (14.15%) groups (Fig. 7K).

Through H&E staining of wound tissue, we further evaluated the anti-inflammatory effects of different patches. Fig. S19A shows that the Blank group still exhibited significant inflammatory cell aggregation in the central wound area on postoperative day 15. Quantitative analysis revealed an inflammatory cell density of approximately 709 cells per 0.1 mm^2 in the Blank group. In contrast, the BC and AMs groups showed reduced densities to approximately 574 cells per 0.1 mm^2 and 559 cells per 0.1 mm^2, respectively. The GBP group exhibited a further significant reduction to 300 cells per 0.1 mm^2 (Fig. S19B). Moreover, we performed immunohistochemical staining of IL-10 and TNF-α in wound tissues on day 15 to evaluate the inflammatory microenvironment (Fig. S20). Compared with the Blank group, the BC, AMs, and GBP groups all showed increased IL-10 expression and decreased TNF-α expression, indicating that the BC-based patch platform alleviated excessive inflammation in diabetic wounds. Specifically, the IL-10-positive rates were 8.07%, 32.19%, 30.95%, and 35.49% in the Blank, BC, AMs, and GBP groups, respectively, while the TNF-α positive rates were 40.25%, 16.04%, 11.31%, and 9.42%, respectively. Among the patch-treated groups, GBP showed the highest IL-10 and lowest TNF-α levels, suggesting a favorable anti-inflammatory microenvironment. These results indicate that the superior wound healing performance of GBP is associated with both inflammation regulation and stable self-powered electrical stimulation, rather than anti-inflammatory activity alone.

The differences in wound healing outcomes can be attributed to the varying mechanisms of each group. The GBP patch, through strong and sustained electrical stimulation, significantly enhances the endogenous electric field, promoting fibroblast migration, proliferation, and collagen synthesis, which accelerates granulation tissue maturation and wound closure. In contrast, while the AMs group provided mild and unstable electrical stimulation, the healing was slower, and granulation tissue formation was less pronounced. The BC/PtNPs and BC groups, with theirs anti-inflammatory and anti-adhesion effects, reduced inflammation and prevented adhesion but lacked electrical stimulation, resulting in slower healing. In contrast, the OC-GBP and Ag/BC groups not only possess anti-inflammatory and anti-adhesion properties but also exhibit antibacterial activity. Consequently, their wound healing efficacy surpasses that of the BC/PtNPs and BC groups. The blank group, with no intervention, had the slowest healing. Collectively, these results indicate that GBP potently enhance both granulation tissue formation and re-epithelialization through electrical stimulation, leading to accelerated repair of diabetic wounds.

Conclusion

In summary, we present a flexible bioelectronic patch powered by GFC with a maze-like oxygen-limiting structure, which integrates high output performance and excellent mechanical flexibility. Using BC as the electrode scaffold, the device exhibits systematic biocompatibility. The developed GFC demonstrates outstanding electrochemical performance—including high catalytic activity and power density—along with operational stability, achieving a peak power density of 96.57 μW cm^{-2}, which exceeds previously reported values for implantable non-biocatalytic GFCs. Furthermore, the GFC shows extended operational durability, maintaining a high voltage output for nearly one week while retaining approximately 87% of its initial performance. In the context of diabetic wound treatment, the GBP synergistically enhances multiple biological processes, such as antibacterial, anti-inflammatory, and anti-adhesion effects, by amplifying the endogenous electric field within the wound, thereby significantly accelerating diabetic wound healing. The GFC-driven flexible electronic patch introduced in this study represents an innovative approach to endogenous electrical stimulation. Compared with conventional electrical stimulation methods, GFC-based endogenous stimulation also improves the local hyperglycemic microenvironment, rendering it particularly suitable for the treatment of diabetic chronic wounds.

This platform can continuously provide electrical stimulation, effectively reducing fibrosis in chronic wounds and postoperative injuries, with potential applications in areas such as intestinal, uterine, neural, tendon, and bone repair, thereby shortening recovery times and improving long-term outcomes. Overall, the proposed GFC patch not only demonstrates significant efficacy in diabetic wound healing but also provides a sustainable electrotherapy paradigm for internal wound treatment requiring adhesion prevention, with broad clinical application potential.

CRediT authorship contribution statement

Ming Yin: Writing – original draft, Visualization, Investigation, Formal analysis, Data curation, Conceptualization. **Xiangxiang Wang:** Methodology, Investigation, Formal analysis, Data curation. **Engui Wang:** Methodology, Investigation, Data curation. **Longfei Li:** Data curation. **Chang Zhu:** Data curation. **Peng Cheng:** Data curation. **Haochen Xie:** Data curation. **Han Ouyang:** Data curation. **Hongqing Feng:** Funding acquisition, Data curation. **Shumin Liu:** Writing – review

& editing, Supervision. **Zhou Li:** Writing – review & editing, Supervision, Project administration, Funding acquisition. **Lingling Xu:** Writing – review & editing, Supervision, Project administration, Conceptualization.

Declaration of competing interest

The authors declare that they have no known competing financial interests or personal relationships that could have appeared to influence the work reported in this paper.

Acknowledgements

The authors thank all the laboratory members for their cooperation in this work. This work was supported by the National Natural Science Foundation of China (T2125003, U25A20417, and 82322037), Beijing Natural Science Foundation (L245015, Z240022, and 25JL006), Hebei Natural Science Foundation (E2019409072).

Appendix A. Supplementary data

Supplementary data to this article can be found online at https://doi.org/10.1016/j.mattod.2026.103380.

Data availability

Data will be made available on request.

References

[1] T.T. Wei, et al., Nat. Nanotechnol. 19 (8) (2024) 1178.
[2] H.X. Xie, et al., Adv. Funct. Mater. 34 (36) (2024) 2401209.
[3] F. Wang, et al., Mater. Today 84 (2025) 48.
[4] N. Singh, et al., JAMA 293 (2) (2005) 217.
[5] Y. Xiong, et al., Cell Death Dis. 16 (1) (2025) 341.
[6] H. Brem, M. Tomic-Canic, J. Clin. Invest. 117 (5) (2007) 1219.
[7] Z. Yu, et al., J. Nanobiotechnol. 23 (1) (2025) 749.
[8] C.D. McCaig, et al., Physiol. Rev. 85 (3) (2005) 943.
[9] R. Luo, et al., Adv. Mater. 35 (16) (2023) 2208395.
[10] M. Zhao, et al., Nature 442 (7101) (2006) 457.
[11] R. Luo, et al., Adv. Healthc. Mater. 10 (16) (2021) 2100557.
[12] E. Wang, et al., Device 3 (6) (2025) 100724.
[13] L. Xu, et al., Device 3 (6) (2025) 100721.
[14] G. Yao, et al., Sci. Bull. 69 (14) (2024) 2289.
[15] J. Liu, et al., Mater. Today 88 (2025) 585.
[16] Y. Zhang, et al., Mater. Today 73 (2024) 179.
[17] W. Li, et al., Adv. Healthc. Mater. 13 (13) (2024) 2304365.
[18] R. Yuan, et al., Small 17 (50) (2021) 2103997.
[19] W. Li, et al., ACS Appl. Mater. Interfaces 17 (46) (2025) 62936.
[20] M. Yin, et al., Adv. Mater. Technol. 11 (5) (2026) e01379.
[21] R. Brendgen, et al., Micro 4 (4) (2024) 530.
[22] M. Hubl, et al., Micro 3 (2) (2023) 521.
[23] X. Zhang, et al., Sci. Adv. 9 (28) (2023) eadh1415.
[24] R. Luo, et al., Adv. Mater. 37 (40) (2025) 2501306.
[25] W. Xu, et al., Mater. Today Bio 34 (2025) 102155.
[26] Y. Sun, et al., Adv. Healthc. Mater. 8 (10) (2019) 1900127.
[27] H. Li, et al., Nat. Commun. 11 (1) (2020) 5437.
[28] H. Yao, et al., Rare Met. 44 (4) (2025) 2513.
[29] T. Lu, et al., Adv. Mech. 38 (4) (2008) 393.
[30] S. Kerzenmacher. Doctoral dissertation, Albert-Ludwigs, of Fribourg-in-Brisgau university, 2010.
[31] S. Liu, et al., RSC Adv. 6 (114) (2016) 112971.
[32] A. Kloke, et al., Fuel Cells 11 (2) (2011) 316.
[33] G. Slaughter, J. Sunday, J. Power Sources 261 (2014) 332.
[34] C.H. Su, et al., J. Taiwan Inst. Chem. Eng. 95 (2019) 48.
[35] C. Gonzalez-Solino, et al., J. Power Sources 472 (2020) 228530.
[36] D. Nnanyelugoh et al., In 2020 IEEE 15th International Conference on Nano/Micro Engineered and Molecular System (NEMS), IEEE (2020) 277.
[37] J. Huang, et al., J. Electrochem. Soc. 168 (6) (2021) 064511.
[38] P. Simons, et al., Adv. Mater. 34 (24) (2022) e2109075.
[39] X. Xu, et al., ACS Appl. Mater. Interfaces 15 (14) (2023) 17969.
[40] Z. Lin, et al., Adv. Mater. 37 (16) (2025) 2416410.
[41] J. Huang, et al., Mater. Horizons 12 (19) (2025) 8033.
[42] C. Zhang, et al., Adv. Funct. Mater. 35 (43) (2025) 2505906.
[43] Z. He, et al., Front. Bioeng. Biotechnol. 9 (2021) 807357.
[44] X. Sun, et al., Anti-adhesive coatings, in: Inamuddin, R. Boddula, M. I. Ahamed, and A. M. Asiri (Eds.), Green adhesives: preparation, properties, and applications, John Wiley & Sons, (2020) 1.
[45] J. Cui, et al., Int. J. Biol. Macromol. 265 (2024) 130994.
[46] M.L. Novak, et al., J. Pathol. 232 (3) (2014) 344.
[47] A. Sindrilaru, K. Scharffetter-Kochanek, Adv. Wound Care 2 (7) (2013) 357.
[48] C. Mondadori, et al., Bioact. Mater. 21 (2023) 209.
[49] L. Li, et al., Sci. Bull. 71 (4) (2026) 857.